Article

Catalytic Performance for CO Methanation over Ni/MCM-41 Catalyst in a Slurry-Bed Reactor

Guoqiang Zhang [1,2], Jinyu Qin [2], Yuan Zhou [1], Huayan Zheng [1,2,*] and Fanhui Meng [2,*]

1   Department of Food Science and Engineering, Moutai Institute, Renhuai 564502, China
2   State Key Laboratory of Clean and Efficient Coal Utilization, Taiyuan University of Technology, Taiyuan 030024, China
*   Correspondence: andyzheng1109@163.com (H.Z.); mengfanhui@tyut.edu.cn (F.M.)

Abstract: The Ni-based catalyst has been intensively studied for CO methanation. Here, MCM-41 is selected as support to prepare xNi/MCM-41 catalysts with various Ni contents and the catalytic performance for CO methanation in a slurry-bed reactor is investigated under different reaction conditions. The CO conversion gradually increases as the reaction temperature or pressure rises. As the Ni content increases, the specific surface area and pore volume of xNi/MCM-41 catalysts decrease, the crystallite sizes of metallic Ni increase, while the metal surface area and active Ni atom numbers firstly increase and then slightly decrease. The 20Ni/MCM-41 catalyst with the Ni content of 20 wt% exhibits the highest catalytic activity for CO methanation, and the initial CH_4 yield rate is well correlated to the active metallic Ni atom numbers. The characterization of the spent xNi/MCM-41 catalysts shows that the agglomeration of Ni metal is accountable for the catalyst deactivation.

Keywords: CO methanation; Ni/MCM-41 catalyst; deactivation; synthetic natural gas; slurry-bed reactor

1. Introduction

Natural gas, primarily consisting of methane, is a highly efficient and clean energy source [1,2]. However, the natural gas reserves are poor in some regions of the world, especially in China, thus the production of synthetic natural gas (SNG) from syngas ($CO + H_2$) has attracted much attention in recent decades [3,4]. Generally, SNG is produced via gasification of coal or biomass, followed by subsequent gas cleaning, conditioning and methanation process. Among them, CO methanation is an essential step [5], and it is a highly exothermic and thermodynamically feasible reaction [6,7]. Due to the poor heat transfer of fixed-bed reactor and the high amount of CO in the syngas, one of the two major challenges in developing the methanation reactor is to remove the highly exothermic heat effectively and in time, and the other is to produce high-efficiency catalysts retaining high catalytic performance at low reaction temperatures.

Aimed at the exothermic characteristics of methanation, a slurry-bed reactor was introduced in the process of CO methanation. In a slurry-bed reactor, catalyst powder suspends in an inert liquid medium, and the system keeps at an isothermal condition because of the high heat transfer coefficients of the liquid medium, which is particularly suitable for the highly exothermic CO methanation reaction, indicating that it can effectively prevent the carbon deposition and catalyst sintering [8–10].

Since 1902, many catalysts, including Ni-, Fe-, Ru- and Co-based catalysts, have been developed to catalyze the methanation reaction [11,12]. Until now, the Ni-based catalyst is still the most commonly-used catalyst to produce SNG due to its good catalytic performance and relatively low price [13,14]. The Ni/Al_2O_3 catalyst was commonly used; however, it was designed particularly for the fixed-bed reactor, and it showed low catalytic activity in a slurry-bed reactor [15]. It has been reported that the catalyst with high Ni dispersion and moderate interactions between Ni species and support exhibited high catalytic activity

for CO methanation. In response to these problems, one of the potential candidates for Ni-based catalysts is to select MCM-41 mesoporous molecular sieve as the support. The reason is that MCM-41 possesses high specific surface area, large pore volume, and homogeneous hexagonal pore array, which can highly disperse the active phase and enhance the metal surface area [16,17]. The Ni-based MCM-41 catalyst with high Ni content and dispersion could be prepared by the incipient wetness impregnation method [18]. It has been reported that the Ni-based MCM-41 catalyst, prepared via a wet impregnation method, exhibited good catalytic activity for naphthalene hydrogenation [19]. Zhang et al. [20] found that the nickel based MCM-41 catalyst showed good activity for syngas methanation in a fixed-bed reactor.

In this work, MCM-41-supported Ni catalysts were prepared via the impregnation method where the Ni content varied from 4 to 28 wt% and the catalytic performance for CO methanation in a slurry-bed reactor was investigated. The obtained catalysts were characterized by N_2 adsorption-desorption, XRD, H_2-TPR, H_2 chemisorption and TEM. The effects of reaction temperature and pressure were studied, and the reason for the catalyst deactivation after reaction was analyzed. The aim is to clarify the relationship between the structures and the catalytic methanation performance.

2. Results and Discussion

2.1. Catalytic Performance for CO Methanation in a Slurry-Bed Reactor

The Ni content greatly affects the catalytic methanation performance. Thus, the methanation performance over xNi/MCM-41 catalysts in a slurry-bed reactor was investigated, and the results are shown in Figure 1. Figure 1a shows that the 4Ni/MCM-41 catalyst exhibits an initial CO conversion of 71.8% which then decreased to 32.1% after a 45 h reaction. As the Ni content increased to 12 wt%, the initial CO conversion of 12Ni/MCM-41 catalyst reached 89.0%; moreover, the stability was also enhanced. Further increasing the Ni content to 20 wt% or 28 wt%, the initial CO conversion reached up to ~94.4%. For comparison, the 20Ni/SiO$_2$ catalyst prepared by using silica as support shows much lower CO conversion than the 20Ni/MCM-41 catalyst. The main gas products during the CO methanation reaction are CH_4, CO_2 and C_{2-4}. Figure 1b–d show the variations in selectivity of CH_4, CO_2, and C_{2-4} as reaction time goes on. It could be found in Figure 1b that the selectivity of CH_4 slightly increased during the reaction, and all the xNi/MCM-41 catalysts exhibit higher CH_4 selectivity than 20Ni/SiO$_2$. Figure 1c shows that the selectivity of CO_2 is in the range of 0.5% and 6.1%, and it slightly decreased during the reaction. Figure 1d shows that the C_{2-4} selectivity of xNi/MCM-41 catalyst was less than 1.8%, and it only slightly changed with the variation in Ni content, whereas the C_{2-4} selectivity of the 20Ni/SiO$_2$ catalyst was significantly higher than that of 20Ni/MCM-41.

For the CO methanation reaction, the active center Ni metal may form the $[Ni(CO)_4]$ specie at low temperature, which deactivated the catalysts [21,22]. Thus, to minimize the generation of $[Ni(CO)_4]$ specie during the methanation reaction, the reaction was generally conducted at the temperatures higher than 250 °C. Figure 2 displays the effect of reaction temperature on catalytic methanation performance over xNi/MCM-41 catalysts. Figure 2a shows that the CO conversion decreased as the temperature decreased, especially when the temperature was lower than 280 °C. The 4Ni/MCM-41 catalyst exhibits an initial CO conversion of 77.5% at 320 °C, and it shows a dramatic and continuous drop when the reaction temperature decreased from 320 °C to 260 °C. Both 20Ni/MCM-41 and 28Ni/MCM-41 catalysts show high catalytic activity and stability when the temperature reached 300 °C or above. However, the activity decreased quickly when the temperature was reduced to 260 °C. The CH_4 selectivity of the xNi/MCM-41 catalyst is relatively stable at each reaction temperature.
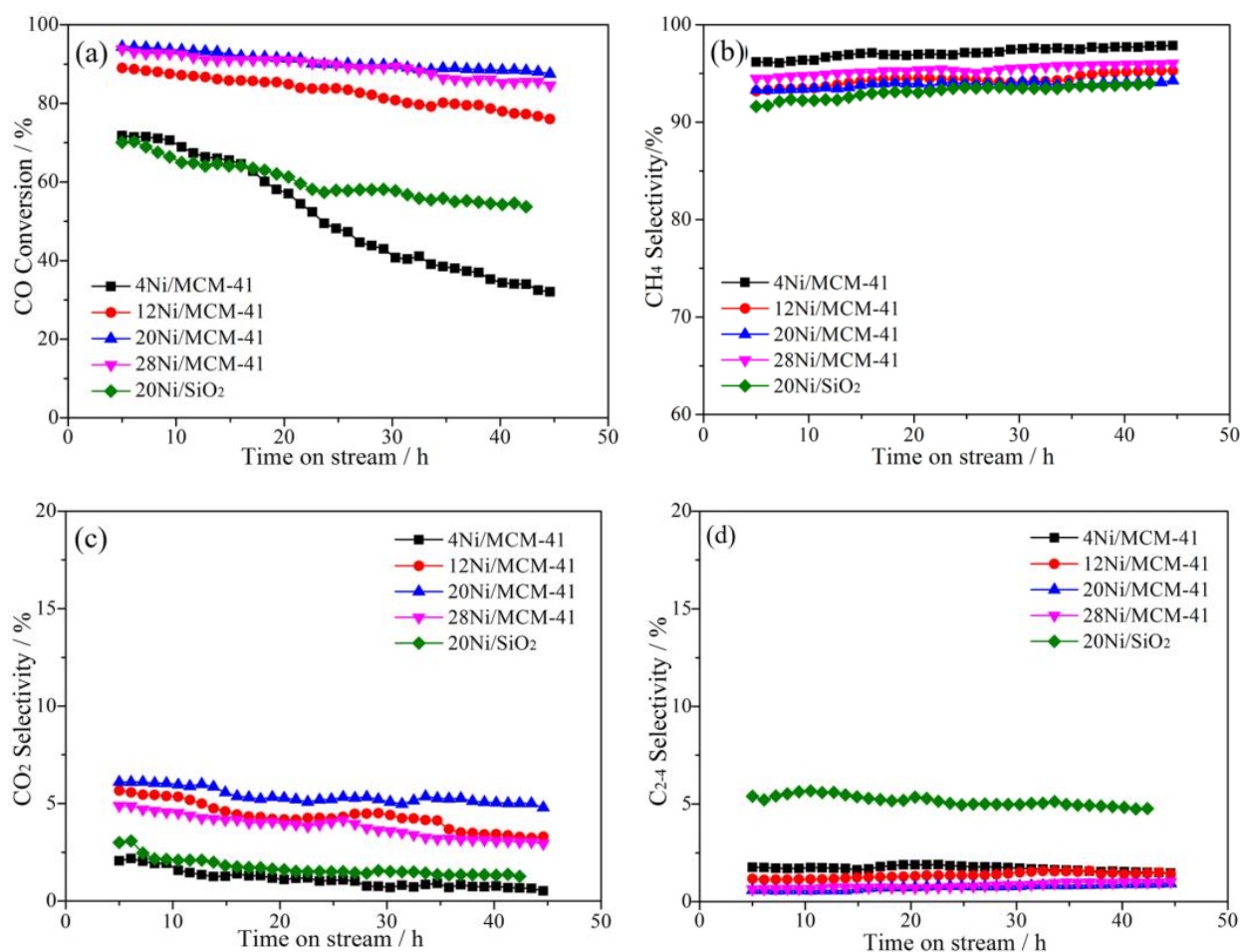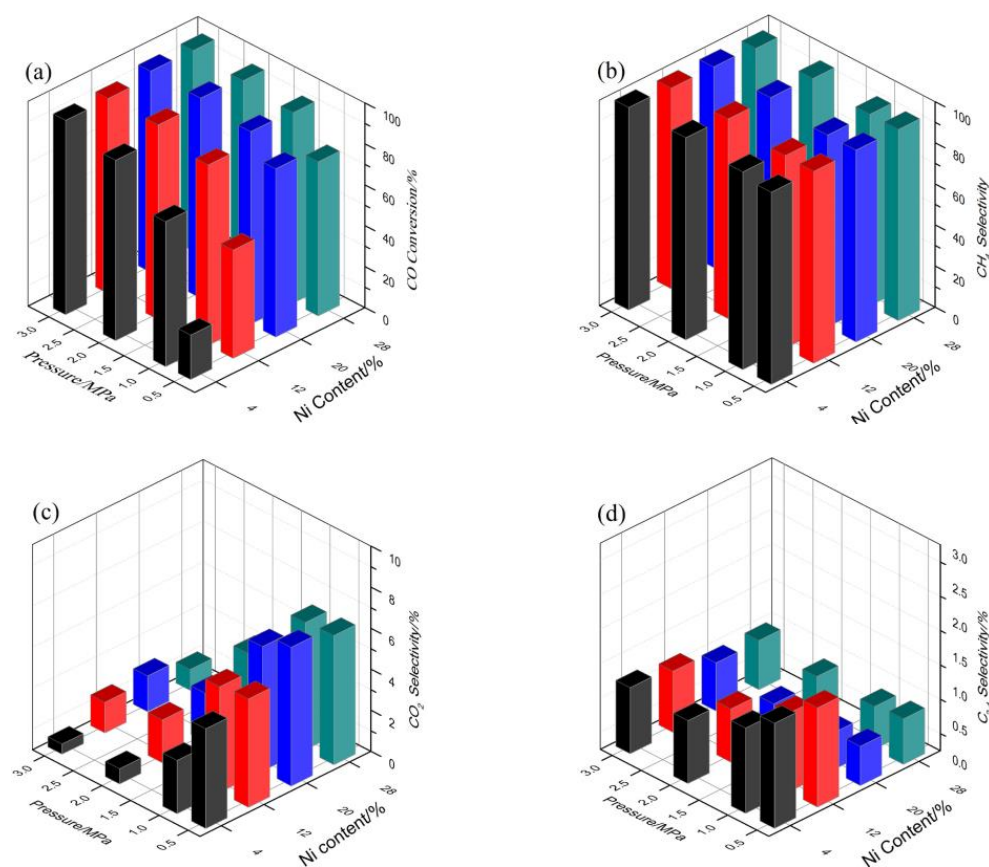
Figure 1. Effect of Ni content on catalytic performance for CO methanation over Ni-based catalysts. (**a**) CO conversion, (**b**) CH_4 selectivity, (**c**) CO_2 selectivity, (**d**) C_{2-4} selectivity. Reaction conditions: 300 °C, 1.0 MPa, and 3000 mL/(g·h).
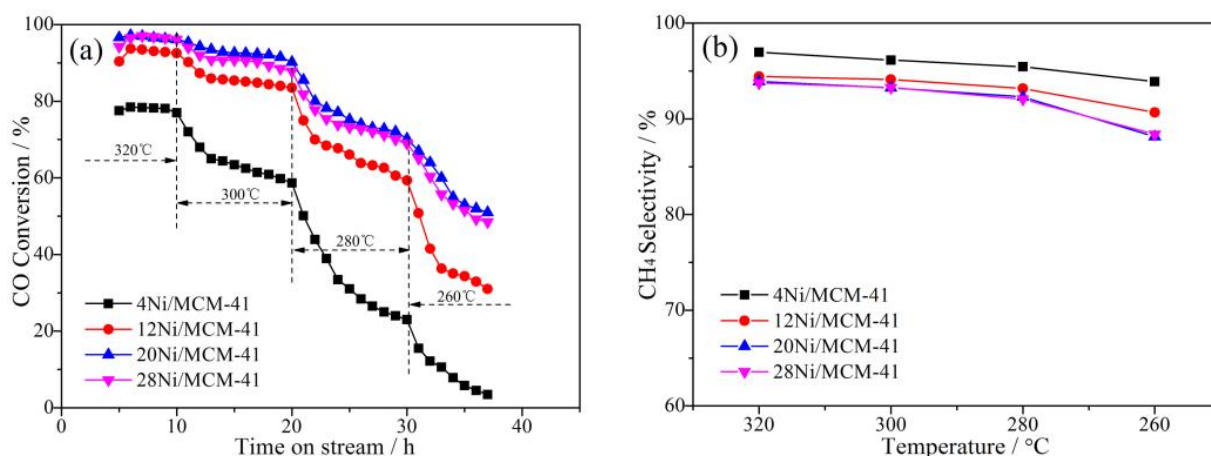
Figure 2. Effect of reaction temperature on catalytic performance for CO methanation over *x*Ni/MCM-41 catalysts. (**a**) CO conversion, (**b**) CH_4 selectivity.

The average value of CH_4 selectivity is displayed in Figure 2b. As the reaction temperature decreased from 320 °C to 260 °C, the selectivity of CH_4 slightly decreased. Furthermore, it is interesting to find that the catalyst with low Ni content exhibits a high CH_4 selectivity, which is probably due to the low Ni content that avoids the side reaction.

The effect of reaction pressure on the catalytic methanation performance over the *x*Ni/MCM-41 catalyst was studied by varying the pressure from 0.5 MPa to 3.0 MPa. The performance tests were carried out at 300 °C and 3000 mL/(g·h), and the results are displayed in Figure 3. Figure 3a shows that the CO conversion increased as the pressure increased from 0.5 MPa to 3.0 MPa. The 4Ni/MCM-41 catalyst exhibited the lowest CO conversion of 21.7% at 0.5 MPa; however, it increased to 94.9% as the pressure increased to 3.0 MPa. When the pressure was 1.0 MPa or higher, the CO conversion of *x*Ni/MCM-41 catalyst slightly increased as the reaction pressure increased.

Figure 3. Effect of reaction pressure on catalytic performance for CO methanation over *x*Ni/MCM-41 catalysts. (**a**) CO conversion, (**b**) CH_4 selectivity, (**c**) CO_2 selectivity, (**d**) C_{2-4} selectivity. Black: 4Ni/MCM-41, red: 12Ni/MCM-41, blue: 20Ni/MCM-41, dark cyan: 28Ni/MCM-41.

Figure 3b shows that the selectivity of CH_4 of all the catalysts exceeded 93.0%, and the selectivity gradually increased as the reaction pressure increased from 0.5 MPa to 3.0 MPa, while the CH_4 selectivity changed slightly as the Ni content increased. This is because the CO methanation is a gas molecular number reducing reaction, where the high pressure could facilitate the positive reaction, which improves the CO conversion and CH_4 selectivity [20]. Figure 3c shows that the selectivity of CO_2 decreased as the reaction pressure was enhanced, and when the pressure reached 2.0 MPa or higher, the selectivity of CO_2 decreased to 3.3% or less. The selectivity of C_{2-4} in Figure 3d was very low, and it changed very slightly as the pressure or Ni content varied.

2.2. Structure and Textural Properties Analysis

X-ray diffraction is one of the most important techniques for characterizing the crystallite size and catalyst structure. Figure 4a shows the wide-angle XRD patterns of MCM-41 support and the calcined Ni-based catalysts. The MCM-41 support exhibits a broad amorphous silica peak at 2θ angles of around 23°, whereas the MCM-41 supported catalysts show diffraction peaks at 2θ of 37.3°, 43.3°, 62.9°, 75.4° and 79.4°, which are assigned to

the characteristic peaks of NiO(111), NiO(200), NiO(220), NiO(311) and NiO(222) (JPCDS, No. 47-1049), respectively. The 4Ni/MCM-41 catalyst exhibits the weakest peak intensity of NiO, indicating the presence of the smallest crystallite size of NiO. As the Ni content increased, the diffraction peaks of NiO become stronger. The crystallite size of NiO at 2θ of 37.3° was estimated using the Scherrer equation, and the results are shown in Table 1. As the Ni content increased, the crystallite sizes of NiO increased, and the 28Ni/MCM-41 catalyst shows the largest crystallite size of 20.9 nm. For comparison, the 20Ni/SiO$_2$ catalyst shows almost the same peak intensity and crystallite size as that of 20Ni/MCM-41.
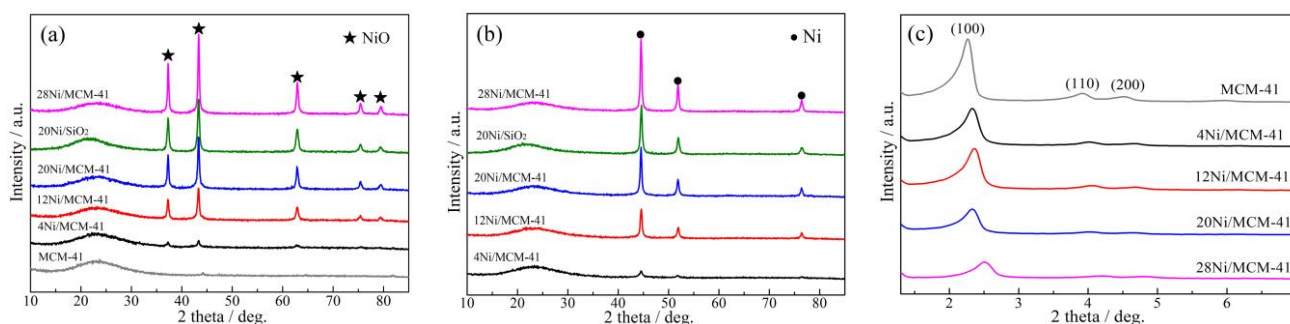
Figure 4. Wide-angle XRD patterns of the (**a**) calcined samples and (**b**) reduced samples, and (**c**) small-angle XRD patterns of calcined samples.

Table 1. Textural properties and crystallite sizes of various samples.

| Catalyst	Specific Surface Area (m²/g) [a]	Pore Volume (cm³/g) [b]	Average Pore Size (nm) [c]	Crystallite Size of NiO/Ni (nm) [d]
MCM-41	1188	1.41	3.1	-
4Ni/MCM-41	979	1.40	3.3	10.7/9.0
12Ni/MCM-41	921	1.39	4.9	15.8/15.6
20Ni/MCM-41	838	1.38	5.2	17.4/17.2
28Ni/MCM-41	804	1.35	5.1	20.9/19.2
20Ni/SiO$_2$	153	1.38	24.1	17.2/16.8

[a] Calculated by BET (Brunauer-Emmett-Teller) equation. [b] BJH (Barret-Joyner-Hallender) desorption pore volume. [c] BJH (Barret-Joyner-Hallender) desorption average pore diameter. [d] calculated from NiO (200) and Ni (111) plane using the Scherrer equation.

Figure 4b shows the XRD patterns of reduced Ni-based catalysts. Each catalyst shows three diffraction peaks at 2θ of 44.5°, 51.9° and 76.4°, which are assigned to Ni(111), Ni(200) and Ni(220) (JPCDS, No. 04-0850), respectively. The peaks of metallic Ni became stronger as the Ni content rose. The crystallite sizes of metallic Ni at 2θ of 44.5° are summarized in Table 1, and it could be found that the crystallite sizes of metallic Ni increased as the Ni content increased.

The low-angle XRD patterns of MCM-41 support and the calcined *x*Ni/MCM-41 catalysts are shown in Figure 4c. Three diffraction peaks were observed for MCM-41 support, indexed as the reflections of (100), (110) and (200) crystal face, characteristic of a highly ordered mesoporous structure with hexagonal pore array [23]. With the increase in Ni content, the (100) peak intensity decreased, and the position of the interplanar spacing of (100) reflection shifts toward higher angles, indicating the decrease of the lattice parameter. The (110) and (200) peaks almost disappeared, which indicates a consequential loss of a long-range order form concerning to the mesopores [24].

N$_2$ adsorption-desorption is a routine technique to probe the texture of porous solids. The isotherms and pore size distributions for MCM-41 support and the reduced *x*Ni/MCM-41 catalysts are presented in Figure 5a,b, respectively. According to the IUPAC nomenclature, the N$_2$ adsorption-desorption isotherms in Figure 5a can be categorized as type IV isotherm, which is typical for the purely siliceous material MCM-41 with mesoporous structure, the hysteresis loops with parallel and almost horizontal branches can be classified as H4-type [25]. A sharp step in the range of relative pressure between 0.2 and 0.4 indicates

that the catalyst possesses uniform mesopores [25,26]. As the Ni content rose, the hysteresis loops of relative pressures p/p_0 changed slightly except the high relative pressures between 0.9 and 1.0, which confirmed that these catalysts have narrow pore size distributions.
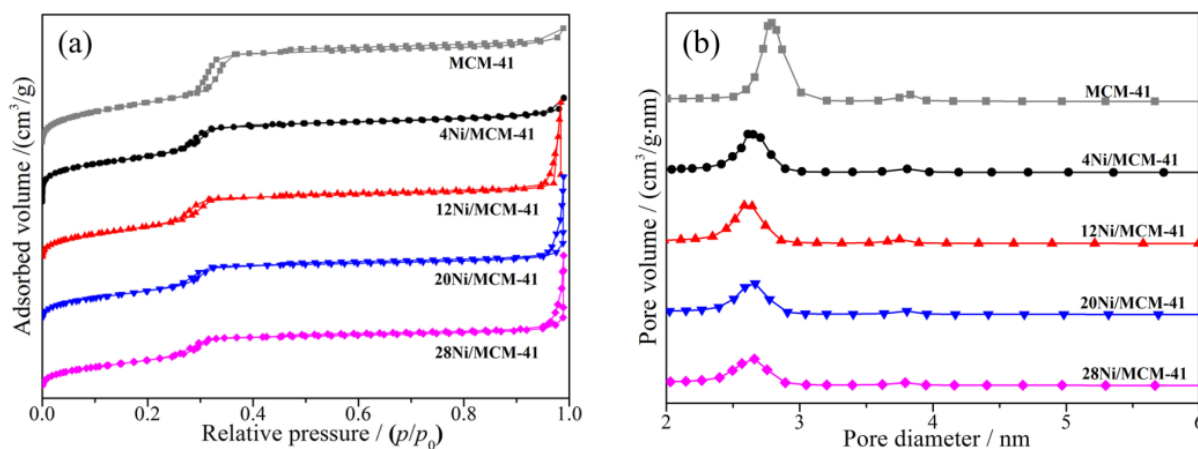

Figure 5. (**a**) Pore size distributions and (**b**) N_2 adsorption-desorption isotherms of MCM-41 support and reduced xNi/MCM-41 catalysts.

Figure 5b shows that all samples exhibit quite narrow pore size distribution mostly in the range of 2 to 4 nm. MCM-41 support shows a large and broad pore size distribution centered at 2.8 nm and a small one centered at 3.8 nm. After the introduction of Ni, the pore size distributions decreased and centered at 2.6 nm; further increasing the Ni content slightly changed the pore size distributions.

The textural properties of MCM-41 support and xNi/MCM-41 catalysts are summarized in Table 1. MCM-41 support possesses the highest specific surface area and pore volume of 1188 m^2/g and 1.41 cm^3/g, respectively, as well as the lowest average pore size of 3.1 nm. While for the xNi/MCM-41 catalysts, the specific surface area and pore volume decreased. The reason is probably due to that the pores were blocked by the Ni species. The average pore size firstly increased and then decreased as the Ni content rose, which was probably due to the accumulation of nickel species existed on the external surface and formed new holes, which led to a textural change in Ni/MCM-41.

2.3. Catalyst Reducibility and Surface Properties Analysis

The catalyst reducibility and metal-support interaction can be characterized by H_2-TPR technique. Figure 6 shows the TPR profiles of calcined catalysts xNi/MCM-41 and 20Ni/SiO$_2$. All catalysts exhibit three reduction peaks, indicating that there were three different interactions between the metal oxide and support [27]. The first peak centered at 310−350 °C could be attributed to the reduction of NiO species, which had no or very weak interaction with MCM-41 support [28]; the second peak around 360−400 °C ascribed to the reduction of bulk NiO [28,29], and the last peak at high temperature could be belonged to the reduction of very small NiO particles and/or NiO species strongly interacted with support [29]. The 4Ni/MCM-41 catalyst shows a very weak peak intensity, and the peak intensity significantly enhanced as the Ni content increased. Moreover, the reduction peaks shift to higher temperatures as the Ni content increased. The 20Ni/MCM-41 catalyst shows reduction peaks at high temperatures, indicating the presence of small NiO particles and/or a strong interaction between the Ni species and MCM-41 support. Generally, the strong interaction between the Ni species and support favors the enhancement of Ni dispersion and the formation of small active Ni particles, which benefits the catalytic activity. The referenced 20Ni/SiO$_2$ catalyst shows a higher reduction temperature compared with 20Ni/MCM-41. Interestingly, the 20Ni/SiO$_2$ catalyst did not present the third reduction peaks at high temperatures, which is probably due to the poor dispersion of NiO species.
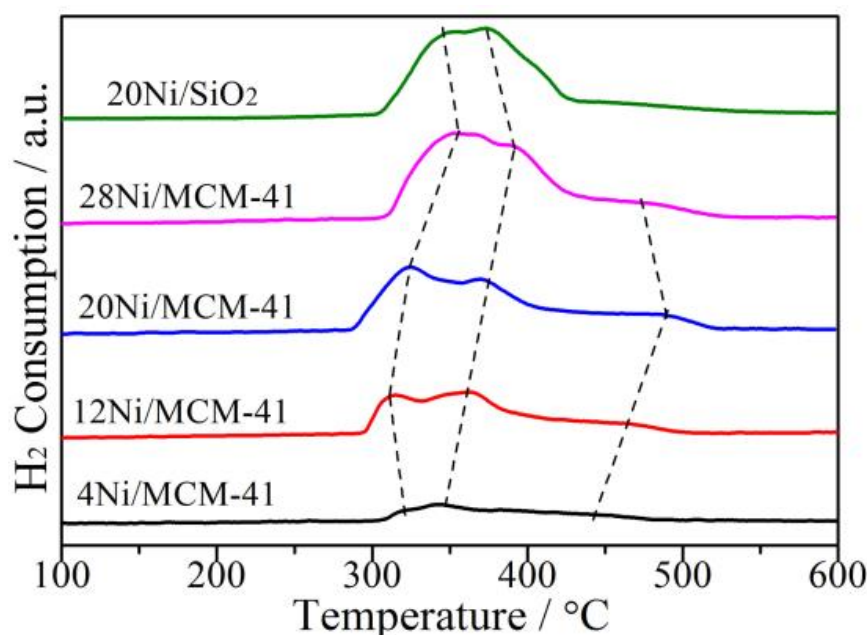
Figure 6. H_2-TPR profiles of calcined xNi/MCM-41 and 20Ni/SiO$_2$ catalysts.

An H_2 chemisorption measurement was conducted to determine the Ni dispersion, metal surface area, number of active Ni atoms and average particle size of Ni. All results were estimated by assuming that one hydrogen atom is adsorbed on one active nickel atom [30,31]. Table 2 shows the H_2 chemisorption results for the reduced xNi/MCM-41 and 20Ni/SiO$_2$ catalysts. Obviously, the Ni dispersion of the xNi/MCM-41 catalysts gradually decreased as the Ni content rose, while the average particle diameter of Ni increased. The results indicate that the active Ni were highly dispersed with small particle size at low Ni contents. The metal surface area and active metallic Ni atom numbers of the catalysts firstly increased and then slightly decreased, indicating that there was an optimum threshold value of Ni content on the MCM-41 support. The 20Ni/SiO$_2$ catalyst shows the Ni dispersion of 1.66% and the values of metal surface area and active metallic Ni atom numbers were all lower than those of 20Ni/MCM-41 catalyst. Among the catalysts tested, the 20Ni/MCM-41 catalyst with a Ni content of 20 wt% shows the highest metal surface area (2.97 m$^2 \cdot$g^{-1}$_{cat}$) and active metallic Ni atom numbers (4.57×10^{19} g^{-1}), which is probably responsible for the high catalytic methanation activity [32].

**Table 2.** H_2 chemisorption results of the reduced xNi/MCM-41 catalysts.

Catalyst	D_{Ni}(%) [a]	S_{cat}(m$^2 \cdot$g^{-1}$_{cat}$) [b]	N_{Ni}($\times 10^{19} \cdot$g^{-1}) [c]	d_H(nm) [d]
4Ni/MCM-41	3.34	0.86	1.32	30.1
12Ni/MCM-41	3.18	2.27	3.49	31.8
20Ni/MCM-41	2.67	2.97	4.57	37.8
28Ni/MCM-41	1.80	2.62	4.04	56.3
20Ni/SiO$_2$	1.66	1.85	2.84	60.7

[a] D_{Ni}: amount of exposed Ni on the surface of the catalysts. [b] S_{cat}: active metal surface area per gram of catalyst. [c] N_{Ni}: numbers of active metallic Ni atom. [d] d_H: average Ni particle size.

TEM technology was employed to observe the catalyst morphology and Ni dispersion. The TEM images of MCM-41 support and representative calcined 4Ni/MCM-41 and 20Ni/MCM-41 catalysts are shown in Figure 7. The TEM image of MCM-41 in Figure 7a exhibits well-ordered mesoporous structure, which was consistent with the results of BET and XRD. Figure 7b shows that the NiO was highly dispersed on MCM-41 and part of NiO was located inside the well-ordered channels pores as clusters or very small nanoparticles. As the Ni content increased up to 20 wt%, the TEM image in Figure 7c exhibits small

NiO particles in the channels of MCM-41 support, which had strong interaction with the support. The result was confirmed by the high temperature reduction peak in H_2-TPR profile. However, parts of NiO particles accumulated and formed large particles on the external surface of the support, which might block the pores and decrease the specific surface areas [33].
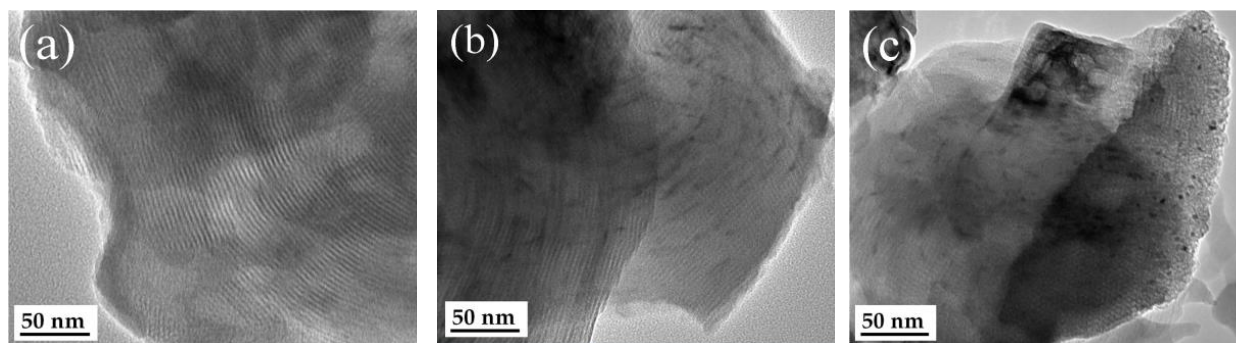
Figure 7. TEM images of MCM-41 support and calcined xNi/MCM-41 catalysts. (**a**) MCM-41 support, (**b**) 4Ni/MCM-41 catalyst, (**c**) 20Ni/MCM-41 catalyst.

2.4. Relationship between Catalytic Activity and Surface Properties

There are many factors affecting the catalytic methanation performance. However, it can be found that the active metallic Ni atom numbers of xNi/MCM-41 catalysts served well as a correlating parameter for the catalytic activity in a slurry-bed reactor. Figure 8 shows the relationship between the active metallic Ni atom numbers and the initial yield rate of CH_4 per mass of xNi/MCM-41 catalyst (r_{CH4}(mmol·h^{-1}·g^{-1})) at 300 °C, 1.0 MPa, and 3000 mL·g^{-1}·h^{-1}. As mentioned above, the initial catalytic activity of CO conversion in Figure 1a firstly increased and then slightly decreased as the Ni content increased, reaching the maximum value at the Ni content of 20 wt%, while the selectivity of CH_4 of each xNi/MCM-41 catalyst kept almost the same value. It should be noted that the initial CH_4 yield rate is well correlated to the active metallic Ni atom numbers (as shown in Table 2). In other words, xNi/MCM-41 catalysts with more amounts of active metallic Ni atom were favorable for improving the catalytic activity. The 20Ni/SiO_2 catalyst exhibited a lower yield rate of CH_4, which was probably due to the poor dispersion of active metallic Ni and the large Ni particles as shown in Table 2.
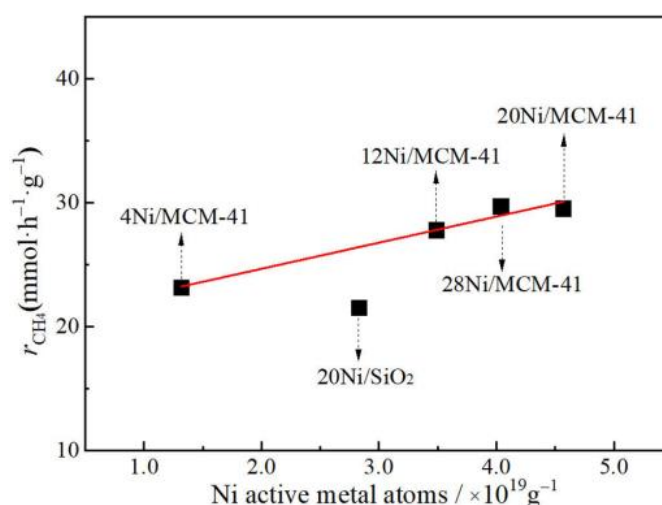

Figure 8. Relationship between the numbers of active Ni atom and initial CH_4 yield rate per unit mass of catalyst at 300 °C.

2.5. Characterization of Spent Catalysts

Figure 9a shows the XRD patterns of spent xNi/MCM-41 catalysts after a reaction time for 45 h. All catalysts exhibit the diffraction peaks at 2θ angles of 44.5°, 51.9°, and 76.4°, corresponding to characteristic peaks of metallic Ni (JPCDS, No. 04-0850), and the peak intensity increased as the Ni content rose. The crystallite sizes of metallic Ni at 2θ of 44.5° are summarized and compared in Table 3. It is found that the Ni crystallite sizes of spent xNi/MCM-41 catalysts slightly larger than those of the freshly reduced ones, especially for the freshly reduced 4Ni/MCM-41catalyst, the increase in Ni crystallite size is probably responsible for the deactivation of xNi/MCM-41 catalysts. The results were confirmed by the TEM image of the spent 20Ni/MCM-41 catalyst in Figure 9b. It is displayed that the Ni particle of the spent 20Ni/MCM-41 catalyst was agglomerated and the particle size was larger than that of the fresh 20Ni/MCM-41 catalyst.
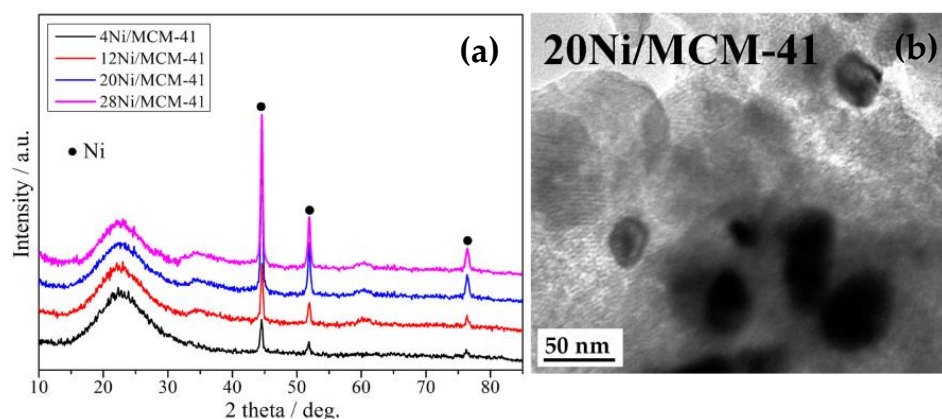
Figure 9. XRD patterns (**a**) and TEM image (**b**) of spent xNi/MCM-41 catalysts after 45 h reaction.

Table 3. Textural properties and Ni crystallite size of fresh and spent xNi/MCM-41 catalysts.

Catalyst	Specific Surface Area (m²/g) [a]	Pore Volume (cm³/g) [b]	Average Pore Size (nm) [c]	Ni Crystallite Size (nm) [d]
4Ni/MCM-41	783	0.78	3.25	9.0/17.7
12Ni/MCM-41	584	0.53	5.00	15.6/21.1
20Ni/MCM-41	488	0.53	4.07	17.2/23.0
28Ni/MCM-41	322	0.50	4.84	19.2/24.1

[a] Calculated by BET (Brunauer-Emmett-Teller) equation. [b] BJH (Barret-Joyner-Hallender) desorption pore volume. [c] BJH (Barret-Joyner-Hallender) desorption average pore diameter. [d] calculated from Ni(111) plane of fresh/spent catalyst using the Scherrer equation.

The textural properties of spent xNi/MCM-41 catalysts are summarized in Table 3. As the Ni content increased, the specific surface area significantly decreased from 783 m²/g for 4Ni/MCM-41 to 322 m²/g for 28Ni/MCM-41. Compared with the textural properties of fresh xNi/MCM-41 catalysts in Table 1, it could be found that the specific surface area and pore volume of spent xNi/MCM-41 catalysts all decreased. The catalyst with high Ni content shows a large decrease, the reason was probably due to the blockage of the micropores of MCM-41 by the agglomeration of Ni species.

3. Materials and Methods

3.1. Catalyst Preparation

The nickel catalysts supported on MCM-41 molecular sieve (supplied by Tianjin Nankai catalyst company, China, 100–200 mesh) were prepared by the incipient wetness impregnation method as follows: first, the MCM-41 was calcined in air at 550 °C for 4 h and used as support. Then, the required amount of $Ni(NO_3)_2 \cdot 6H_2O$ (purchased from Sinopharm mbcvx, and used without further treatment) was completely dissolved in a certain amount of distilled water, and followed by addition of 10.0 g of MCM-41, the

resulting mixture was sealed with plastic film to avoid the quick evaporation of water and stirred continuously at room temperature for 24 h. Finally, the mixture was held at 80 °C for 5 h and dried at 120 °C for 12 h, and then calcined in air at 550 °C for 4 h at a heating rate of 2 °C·min^{-1} to form NiO/MCM-41; the obtained samples were designated as xNi/MCM-41 catalysts, where x represents the weight content of metallic Ni (4 wt%, 12 wt%, 20 wt%, and 28 wt%). For comparison, the 20Ni/SiO$_2$ catalyst with the Ni content of 20 wt% was prepared by the impregnation method as described above by using silica (Degussa, Aerosil 200) as support.

3.2. Catalyst Characterization

The N$_2$ adsorption-desorption measurement was performed by a Beishide 3H-2000PS specific surface and pore size analyzer, using N$_2$ as the adsorbing medium at −196 °C. Prior to the test, the sample was degassed at 250 °C for 3 h. The BET surface area was determined by the Brunauer-Emmett-Teller (BET) method, the average pore diameter was evaluated with the Barrett-Joyner-Halenda (BJH) method using the desorption isotherm branch.

X-ray diffraction (XRD) data were obtained on DX-2800A diffractometer (Dandong, China) with a scanning step of 4°/min using the $K\alpha$ radiation of Cu (λ = 0.154056 nm) at 40 kV and 30 mA. The crystallite size of Ni metal or NiO was calculated using the Scherrer equation.

Temperature-programmed reduction of H$_2$ (H$_2$-TPR) was carried out on a Micromeritics Autochem II 2920 instrument (Micromeritics Instrument Corporation, Atlanta, USA). Prior to the measurement, 20 mg of the sample was pretreated in flowing He (50 mL/min) at 350 °C for 0.5 h, after cooling down to room temperature, the He was switched to 10%H$_2$/90%Ar (50 mL/min) and heated at 800 °C at a heating rate of 10 °C/min.

The H$_2$-chemisorption experiment was also conducted on a Micromeritics Autochem II 2920 instrument (Micromeritics Instrument Corporation, Atlanta, USA). Prior to the test, 200 mg of the sample was reduced by flowing 10%H$_2$/90%Ar at 550 °C for 2 h, then the sample was cooled down to 50 °C and the loop 10%H$_2$/90%Ar gas was pulsed over the sample and the TCD signals were recorded until the peak area remain constant. A 5 µL loop was used for this purpose and the loop was calibrated to determine its precise volume under local conditions. The metallic Ni surface area and Ni dispersion were calculated by assuming that one hydrogen atom occupies one surface metallic Ni atom [31]. The Ni dispersion, metal surface area, number of active nickel atoms and average particle size of Ni are calculated from Equations (1)–(4), respectively:

$$D_{\mathrm{Ni}}(\%) = \left(\frac{V_{\mathrm{ad}}}{V_{\mathrm{m}}}\right) \times \left(\frac{\mathrm{SF} \times \mathrm{M_{Ni}}}{W_{\mathrm{s}} \times F_{\mathrm{Ni}}}\right) \times 100\% \tag{1}$$

$$S_{\mathrm{cat}}\left(\mathrm{m}^2/\mathrm{g_{cat}}\right) = \frac{V_{\mathrm{ad}}}{W_{\mathrm{s}} \times V_{\mathrm{m}}} \times \mathrm{SF} \times \mathrm{N_A} \times \mathrm{R_A} \tag{2}$$

$$N_{\mathrm{Ni}}(\mathrm{Ni\ atoms/mol}) = \frac{V_{\mathrm{ad}}}{W_{\mathrm{s}} \times V_{\mathrm{m}}} \times \mathrm{SF} \times \mathrm{N_A} \tag{3}$$

$$d_{\mathrm{H}}(\mathrm{nm}) = 6 \times 10^3 / (S_{\mathrm{cat}}/F \times \mathrm{Ni}\rho_{\mathrm{Ni}}) \tag{4}$$

where V_{ad} = volume of H$_2$ chemisorbed at STP (mL) to form a monolayer, V$_{\mathrm{m}}$ = molar volume of H$_2$ gas (22,414 mL/mol), SF = stoichiometric factor, i.e., Ni:H atomic ratio in the chemisorption, which is taken as 1; M$_{\mathrm{Ni}}$ = formula weight of Ni (58.69 g/mol), W_{s} = weight of the sample (g), F_{Ni} = weight percentage of Ni in the sample. S_{cat} = active metal atom; N$_{\mathrm{A}}$ = 6.023 × 10^{23}; R$_{\mathrm{A}}$ is the atomic cross-sectional area of Ni, which is 0.0649 nm^2; ρ_{Ni} = density of Ni metal (8.9 g/cm^3).

Transmission electron microscopy (TEM) was performed on JEOL JEM-2100F microscope (Tokyo, Japan) operated at 200 kV. Prior to the measurement, the solid was dispersed in ethanol, ultrasonicated and deposited on a sample holder.

3.3. Catalyst Performance Evaluation

The catalyst was firstly reduced at 550 °C for 6 h in a flow of 25% H_2 diluted with N_2, and then used for activity test. The CO methanation reaction was carried out in a 250 mL slurry-bed reactor (Dalian Tongda Reactor Factory, Dalian, China). In each experiment, 2.0 g of reduced catalyst and 120 mL of paraffin were introduced into the reactor and rotated at a speed of 750 r/min. N_2 was used to purge the air, and then the syngas of H_2 and CO was switched as feed gas. The reaction was performed at H_2/CO molar ratio of 3:1 and 3000 mL/g_{cat}·h in the temperature range of 260–320 °C with the interval of 20 °C. The gas products were firstly cooled down at 2 °C, the cooled liquid was then removed in a gas-liquid separator, the outlet gas was quantitatively analyzed by an online gas chromatography (Agilent 7890A), which was equipped with a flame ionization detector (FID) and a thermal conductivity detector (TCD) using He (99.999%) as the carrier gas. The HP-AL/S column was used to analyze CH_4 and $C_{2–4}$, while Porapak-Q column, HP-PLOT/Q column and HP-MOLESIEVE column were used to analyze CO, N_2 and CO_2.

The CO conversion, CH_4, CO_2, and $C_{2–4}$ selectivity were calculated as follows:

$$X_{CO} = \frac{F(CO_{in}) - F(CO_{out})}{F(CO_{in})} \times 100\% \tag{5}$$

$$S_{CH4} = \frac{F(CH_{4,\,out})}{F(CO_{in}) - F(CO_{out})} \times 100\% \tag{6}$$

$$S_{CO2} = \frac{F(CO_{2,\,out})}{F(CO_{in}) - F(CO_{out})} \times 100\% \tag{7}$$

$$S_{Ci} = \frac{i \times F(C_{i,\,out})}{F(CO_{in}) - F(CO_{out})} \times 100\% \; (i = 2,\,3,\,4) \tag{8}$$

where X_{CO}, S_{CH4}, S_{CO2} and S_{Ci} represent the CO conversion, the CH_4, CO_2, and $C_{2–4}$ selectivity, respectively. $C_{2–4}$ represents the hydrocarbons contain 2 to 4 carbons. *F* represents the volume flow of CO, CH_4, and CO_2 (mL/min, *STP*), respectively.

4. Conclusions

*x*Ni/MCM-41 catalysts with various Ni contents were prepared by the impregnation method, and applied for CO methanation in a slurry-bed reactor. As the Ni content increased, the specific surface area and pore volume of *x*Ni/MCM-41 catalysts decreased, the crystallite size of metallic Ni increased, whereas the metal surface area and active Ni atom numbers firstly increased and then slightly decreased. The 20Ni/MCM-41 catalyst with the Ni content of 20 wt% exhibited the highest catalytic activity for CO methanation, and the initial CH_4 yield rate was well correlated to the active metallic Ni atom numbers. Moreover, the 20Ni/MCM-41 catalyst shows much higher activity than the referenced 20Ni/SiO_2 catalyst. The results of the optimization of reaction conditions show that the CO conversion gradually increases as the reaction temperature or pressure rises. The deactivation of *x*Ni/MCM-41 catalysts was attributed to the agglomeration of Ni.

Author Contributions: Conceptualization, F.M.; methodology, G.Z. and J.Q.; software, J.Q. and F.M.; formal analysis, J.Q.; investigation, G.Z., J.Q. and Y.Z.; data curation, F.M.; writing—review and editing, F.M.; supervision, F.M. and H.Z.; funding acquisition, G.Z. H.Z. and F.M. All authors have read and agreed to the published version of the manuscript.

Data Availability Statement: The data presented in this study are available on request from the corresponding author.

Conflicts of Interest: The authors declare no conflict of interest.

References

1. Zeng, Y.; Ma, H.; Zhang, H.; Ying, W.; Fang, D. Ni-Ce-Al composite oxide catalysts synthesized by solution combustion method: Enhanced catalytic activity for CO methanation. *Fuel* **2015**, *162*, 16–22. [CrossRef]
2. Li, J.; Li, P.; Li, J.; Tian, Z.; Yu, F. Highly-dispersed Ni-NiO nanoparticles anchored on an SiO_2 support for an enhanced CO methanation performance. *Catalysts* **2019**, *9*, 506. [CrossRef]
3. Meng, F.; Li, X.; Lv, X.; Li, Z. CO hydrogenation combined with water-gas-shift reaction for synthetic natural gas production: A thermodynamic and experimental study. *Int. J. Coal Sci. Technol.* **2018**, *5*, 439–451. [CrossRef]
4. Hatta, A.H.; Jalil, A.A.; Hassan, N.S.; Hamid, M.Y.S.; Rahman, A.F.A.; Teh, L.P.; Prasetyoko, D. A review on recent bimetallic catalyst development for synthetic natural gas production via CO methanation. *Int. J. Hydrog. Energy* **2022**, *47*, 30981–31002. [CrossRef]
5. Xu, B.; Meng, X.; Xin, Z.; Gao, W.; Yang, D.; Jin, D.; Zhao, R.; Dai, W. A novel CO methanation catalyst system based on acid-etched natural halloysites as supports. *Ind. Eng. Chem. Res.* **2022**, *61*, 13328–13340. [CrossRef]
6. Shinde, V.M.; Madras, G. CO methanation toward the production of synthetic natural gas over highly active Ni/TiO_2 catalyst. *AIChE J.* **2014**, *60*, 1027–1035. [CrossRef]
7. Liu, S.-S.; Jin, Y.-Y.; Han, Y.; Zhao, J.; Ren, J. Highly stable and coking resistant Ce promoted Ni/SiC catalyst towards high temperature CO methanation. *Fuel Process. Technol.* **2018**, *177*, 266–274. [CrossRef]
8. Zhang, J.; Bai, Y.; Zhang, Q.; Wang, X.; Zhang, T.; Tan, Y.; Han, Y. Low-temperature methanation of syngas in slurry phase over Zr-doped Ni/γ-Al_2O_3 catalysts prepared using different methods. *Fuel* **2014**, *132*, 211–218. [CrossRef]
9. Meng, F.; Li, Z.; Liu, J.; Cui, X.; Zheng, H. Effect of promoter Ce on the structure and catalytic performance of Ni/Al_2O_3 catalyst for CO methanation in slurry-bed reactor. *J. Nat. Gas Sci. Eng.* **2015**, *23*, 250–258. [CrossRef]
10. Ji, K.; Meng, F.; Xun, J.; Liu, P.; Zhang, K.; Li, Z.; Gao, J. Carbon deposition behavior of Ni catalyst prepared by combustion method in slurry methanation reaction. *Catalysts* **2019**, *9*, 570. [CrossRef]
11. Mills, G.A.; Steffgen, F.W. Catalytic methanation. *Catal. Rev.* **1974**, *8*, 159–210. [CrossRef]
12. Somorjai, G.A. The catalytic hydrogenation of carbon monoxide. The formation of C1 hydrocarbons. *Catal. Rev.* **1981**, *23*, 189–202. [CrossRef]
13. Guo, C.; Wu, Y.; Qin, H.; Zhang, J. CO methanation over ZrO_2/Al_2O_3 supported Ni catalysts: A comprehensive study. *Fuel Process. Technol.* **2014**, *124*, 61–69. [CrossRef]
14. Zhang, J.; Jia, X.; Liu, C.-J. Structural effect of Ni/TiO_2 on CO methanation: Improved activity and enhanced stability. *RSC Adv.* **2022**, *12*, 721–727. [CrossRef]
15. Meng, F.; Li, X.; Li, M.; Cui, X.; Li, Z. Catalytic performance of CO methanation over La-promoted Ni/Al_2O_3 catalyst in a slurry-bed reactor. *Chem. Eng. J.* **2017**, *313*, 1548–1555. [CrossRef]
16. Shen, S.; Chen, J.; Koodali, R.T.; Hu, Y.; Xiao, Q.; Zhou, J.; Wang, X.; Guo, L. Activation of MCM-41 mesoporous silica by transition-metal incorporation for photocatalytic hydrogen production. *Appl. Catal. B* **2014**, *150–151*, 138–146. [CrossRef]
17. Yang, M.; Lingjun, Z.; Xiaonan, Z.; Prasert, R.; Shurong, W. CO_2 methanation over nickel-based catalysts supported on MCM-41 with in situ doping of zirconium. *J. CO2 Util.* **2020**, *42*, 101304. [CrossRef]
18. Lensveld, D.J.; Gerbrand Mesu, J.; Jos van Dillen, A.; de Jong, K.P. Synthesis and characterisation of MCM-41 supported nickel oxide catalysts. *Microporous Mesoporous Mater.* **2001**, *44–45*, 401–407. [CrossRef]
19. Qiu, S.; Zhang, X.; Liu, Q.; Wang, T.; Zhang, Q.; Ma, L. A simple method to prepare highly active and dispersed Ni/MCM-41 catalysts by co-impregnation. *Catal. Commun.* **2013**, *42*, 73–78. [CrossRef]
20. Zhang, J.; Xin, Z.; Meng, X.; Tao, M. Synthesis, characterization and properties of anti-sintering nickel incorporated MCM-41 methanation catalysts. *Fuel* **2013**, *109*, 693–701. [CrossRef]
21. Zyryanova, M.M.; Snytnikov, P.V.; Gulyaeva, R.V.; Amosov, Y.I.; Boronin, A.I.; Sobyanin, V.A. Performance of Ni/CeO_2 catalysts for selective CO methanation in hydrogen-rich gas. *Chem. Eng. J.* **2014**, *238*, 189–197. [CrossRef]
22. Munnik, P.; Velthoen, M.E.Z.; de Jongh, P.E.; de Jong, K.P.; Gommes, C.J. Nanoparticle growth in supported nickel catalysts during methanation reaction—Larger is better. *Angew. Chem. Int. Ed.* **2014**, *53*, 9493–9497. [CrossRef] [PubMed]
23. Carraro, P.; Elías, V.; García Blanco, A.; Sapag, K.; Moreno, S.; Oliva, M.; Eimer, G. Synthesis and multi-technique characterization of nickel loaded MCM-41 as potential hydrogen-storage materials. *Microporous Mesoporous Mater.* **2014**, *191*, 103–111. [CrossRef]
24. Park, S.J.; Lee, S.Y. A study on hydrogen-storage behaviors of nickel-loaded mesoporous MCM-41. *J. Colloid. Interf. Sci.* **2010**, *346*, 194–198. [CrossRef] [PubMed]
25. Carraro, P.; Elías, V.; Blanco, A.A.G.; Sapag, K.; Eimer, G.; Oliva, M. Study of hydrogen adsorption properties on MCM-41 mesoporous materials modified with nickel. *Int. J. Hydrog. Energy* **2014**, *39*, 8749–8753. [CrossRef]
26. Lehmann, T.; Wolff, T.; Hamel, C.; Veit, P.; Garke, B.; Seidel-Morgenstern, A. Physico-chemical characterization of Ni/MCM-41 synthesized by a template ion exchange approach. *Microporous Mesoporous Mater.* **2012**, *151*, 113–125. [CrossRef]

27. Tao, M.; Meng, X.; Xin, Z.; Bian, Z.; Lv, Y.; Gu, J. Synthesis and characterization of well dispersed nickel-incorporated SBA-15 and its high activity in syngas methanation reaction. *Appl. Catal. A* **2016**, *516*, 127–134. [CrossRef]

28. Zhang, Q.; Wang, T.; Li, B.; Jiang, T.; Ma, L.; Zhang, X.; Liu, Q. Aqueous phase reforming of sorbitol to bio-gasoline over Ni/HZSM-5 catalysts. *Appl. Energy* **2012**, *97*, 509–513. [CrossRef]

29. van de Loosdrecht, J.; van der Kraan, A.M.; van Dillen, A.J.; Geus, J.W. Metal-support interaction: Titania-supported and silica-supported nickel catalysts. *J. Catal.* **1997**, *170*, 217–226. [CrossRef]

30. Meng, F.; Li, X.; Shaw, G.M.; Smith, P.J.; Morgan, D.J.; Perdjon, M.; Li, Z. Sacrificial carbon strategy toward enhancement of slurry methanation activity and stability over Ni-Zr/SiO$_2$ catalyst. *Ind. Eng. Chem. Res.* **2018**, *57*, 4798–4806. [CrossRef]

31. Meng, F.; Wang, L.; Li, X.; Perdjon, M.; Li, Z. Mesoporous nano Ni-Al$_2$O$_3$ catalyst for CO$_2$ methanation in a continuously stirred tank reactor. *Catal. Commun.* **2022**, *164*, 106437. [CrossRef]

32. Jia, C.; Gao, J.; Li, J.; Gu, F.; Xu, G.; Zhong, Z.; Su, F. Nickel catalysts supported on calcium Titanate for enhanced CO methanation. *Catal. Sci. Technol.* **2013**, *3*, 490–499. [CrossRef]

33. Wu, C.; Wang, L.; Williams, P.T.; Shi, J.; Huang, J. Hydrogen production from biomass gasification with Ni/MCM-41 catalysts: Influence of Ni content. *Appl. Catal. B* **2011**, *108–109*, 6–13. [CrossRef]